Impact of grain-dependent boron uptake on the nano-electrical and local optical properties of polycrystalline boron doped CVD diamond

A.S. Nikolenko[1], P.M. Lytvyn[1], V.V. Strelchuk[1], I.M. Danylenko[1], S.V. Malyuta[1,3], Ya.Ya. Kudryk[1], Yu.Yu. Stubrov[1], T.V. Kovalenko[2], S.O. Ivakhnenko[2]

[1]*V. Lashkaryov Institute of Semiconductor Physics, NAS of Ukraine, 41, prosp. Nauky, 03680 Kyiv, Ukraine*
[2]*V. Bakul Institute for Superhard Materials, NAS of Ukraine, 2, Avtozavodska str. 04074 Kyiv, Ukraine*
[3]*National Technical University of Ukraine "Igor Sikorsky Kyiv Polytechnic Institute"*
37, prosp. Peremohy, 03056 Kyiv, Ukraine
[*]*Corresponding author e-mail: nikolenko@isp.kiev.ua*

Abstract. Boron-doped diamond (BDD) films grown by chemical vapor deposition (CVD) exhibit unique electrical and optical properties owing to the non-uniform uptake of boron dopants across grains. This study utilizes scanning probe microscopy and confocal microspectroscopy techniques to elucidate the influence of grain-dependent boron incorporation on the nano-electrical and local optical characteristics of polycrystalline BDD. The CVD-grown BDD film contained crystallites up to tens of microns, while the surface comprised 200…800 nm grains. Scanning spreading resistance microscopy (SSRM) revealed significant nanoscale resistance variations among individual grains, attributable to differential boron distributions. No distinct grain boundary features were discernible in SSRM data, likely due to the high boron doping of $\sim 3 \cdot 10^{19}\,\text{cm}^{-3}$. SSRM of the Au surface of a BDD/Ti/Pd/Au contact indicated a comparable granular morphology but three orders lower resistance. A network of more resistive grain boundaries was evident, modulated by underlying BDD grain clusters. Photoluminescence spectroscopy showed characteristic bands of nitrogen-vacancy centers and donor-acceptor pairs. Confocal Raman and photoluminescence mapping elucidated substantial spatial heterogeneity in micrometer-scale grains regarding crystal quality, boron and nitrogen concentrations, related to preferential incorporation. The observed peculiarities in BDD's structural and nano-electrical characteristics stem from inherent growth inhomogeneities and grain-dependent boron uptake influenced by defects and strain fields modifying local chemical potentials. This multifaceted nanoscale examination provides critical insights into optimizing electrical and optical properties of BDD films by controlling synthesis conditions and minimizing defects for tailored performance in electronic, electrochemical, and quantum applications.

Keywords: boron-doped CVD diamond, photoluminescence, Raman spectroscopy, conductive atomic force microscopy, optical, electrical and structural properties.

1. Introduction

Polycrystalline boron-doped diamond films, synthesized using the chemical vapor deposition (CVD) technique, have been the focus of extensive research due to their unique electrical and optical properties. These properties that are influenced by the grain-dependent boron uptake, make boron-doped diamond films suitable for a wide range of applications, including micro/nano-electronic devices, photoelectrochemical conversion of CO_2, and as active or heat dissipation layers on electronic devices [1, 2]. Boron-doped diamond (BDD) films have shown great potential in electronics. The wide potential window – outstanding robustness, low capacitance and resistance to fouling of BDD – make it an attractive material for developing electronic devices. For instance, BDD

electrodes have been employed in promising applications like electrochemical sensing, electron field emission devices and electrodes for constructing super-capacitors [3]. Boron-doped diamond films can also be used in quantum computing and information processing applications. Introducing the impurities, such as boron and nitrogen, into the diamond can form color centers, acting as single-photon sources for quantum computing and quantum information processing [3]. In electrochemistry, BDD has been used extensively due to its intriguing properties. BDD is the mechanically most robust electrode material available to electrochemists.

In addition, when the diamond surface is hydrogen-terminated, the diamond conduction band edge lies above the vacuum level, resulting in a negative electron affinity (NEA). This property allows the diamond to act as a solid-state electron emitter, forming solvated electrons under UV light illumination. These solvated electrons can be termed a green, universal reducing agent with high power. Heavily boron-doped, nanostructured diamond electrodes with enhanced light absorption have been developed for the photoelectrochemical conversion of CO_2 under solar illumination. These electrodes have shown high formic acid production rates at low catalyst deposition times and increased catalyst stability on the diamond surface [2]. Boron-doped diamond electrodes are widely used for electrochemical water treatment. Oxidation of water on these electrodes can occur *via* an alternative pathway, producing the hydroxyl radical, which is desirable for water treatment applications [4].

Boron acts as a *p*-type dopant in diamond, introducing positively charged holes into the diamond crystal lattice, thereby making the diamond to be conductive. The degree of conductivity is directly related to the boron concentration; at a doping concentration of around 10^{18} cm^{-3}, the insulating diamond transforms into a semiconducting diamond, and at the concentrations above 10^{21} cm^{-3}, diamond becomes metallic [3, 5–7]. Intermediate doping ($10^{19}…10^{20}$ cm^{-3}) causes nearest neighbor hopping conduction. The boron dopant distribution within individual grains of a diamond film can vary, leading to local property variations. For instance, areas with a higher concentration of boron dopants may exhibit different electrical and optical properties compared to areas with a lower concentration of dopants. Boron incorporation is not uniform across polycrystalline films due to differential uptake in grains with different orientations. Boron incorporates preferentially into (111) oriented grains as compared to (100) grains by a factor of ~10 [6–8]. This results in variations in electrical conductivity and electrochemical activity between differently oriented grains. At low doping, boron substitutes for carbon in the lattice. Boron also goes into interstitial sites at higher doping and accumulates at defects. High levels of doping damage crystal structure integrity. Raman spectroscopy shows decreased intensity and increased FWHM of the diamond peak, indicating more disorder with higher B-doping

[3, 9]. Boron atoms can accumulate at grain boundaries, leading to changes in the electrical and electrochemical properties of the material. However, the exact effects can depend on the specific characteristics of the grain boundaries and the surrounding material [6, 10]. The boron doping process can also lead to formation of defects within the diamond lattice, such as dislocations and twin boundaries. These defects can further influence the material properties, often leading to an increase in the content of localized sp^2-bonds in diamond, which can affect the material electrical and optical properties [11].

The ability to manipulate the electrical properties of CVD diamond films *via* boron doping has introduced numerous opportunities in electronics, electrochemistry and photonics. However, comprehensive research is required to elucidate the effect of grain-dependent boron uptake on these films' nano-electrical and local optical characteristics. Such comprehension is pivotal for optimizing devices that employ boron-doped CVD diamond films and broadening their application spectrum.

Despite the significant advancements, there remains to be more literature addressing the peculiarities of the structural, optical, and electrical attributes of BDD at the single-grain level. However, the feasibility of nanoscale characterization of micro/nanocrystalline BDD films using a scanning probe microscope (SPM) has been substantiated. Conductive atomic force microscopy (AFM) delineates current distribution, indicating grain disparities [6, 7, 10]. Kelvin probe force microscopy (KPFM) has revealed grain work function variations [3, 6]. The relationship between seed density, doping, and interfacial electrical resistance has been ascertained *via* scanning spreading resistance microscopy (SSRM) [12, 13]. Additionally, the influence of elevated temperatures on the oxidation processes of heavily boron-doped diamond electrodes was assessed, and a bimodal nature of BDD conductivity, marked by a progressive rise in the proportion of low conductivity zones, was detected using SRRM, dependent on the BDD crystallographic structure [14].

Photoluminescence (PL) spectroscopy is often used to study diamond structural defects and complexes [15, 16]. Micro-PL mapping, in particular, was used to study the spatial distribution of defects, such as SiV [17] and NV [18–20] centers in CVD diamond films and non-epitaxial diamond inclusions. Micro-Raman spectroscopy was applied earlier to estimate the incorporation of boron to different crystal faces of polycrystalline CVD-diamond [21], to detect secondary phases of graphite and amorphous carbon at grain boundaries [22], and to study the development of elastic strains [23, 24].

This paper is aimed to delve into the impact of grain-dependent boron uptake on the nano-electrical and local optical properties of these polycrystalline boron-doped CVD diamond films using coplanar scanning probe microscopy and micro-Raman/photoluminescence spectroscopy.

Nikolenko A.S., Lytvyn P.M., Strelchuk V.V. et al. Impact of grain-dependent boron uptake on the nano-electrical …

377

2. Experimental details

The boron-doped *p*-type polycrystalline diamond films were grown on a Si substrate using the microwave plasma CVD method (MPCVD). The resultant diamond film exhibited moderate boron doping, reaching concentrations up to $2.8 \cdot 10^{19}$ at./cm^3 as determined using secondary ion mass spectrometry (SIMS). The film presented a columnar crystalline structure with a {110} texture orientation. The average crystallite size was 60 µm with a standard deviation close to 20 µm. Subsequently, the silicon substrate underwent a chemical etching process, producing a free-standing diamond wafer. This wafer was then thinned and polished to achieve an RMS of 15 nm, resulting in a final thickness of 100 µm. Subsequently, to conduct electrical studies [25, 26], ohmic Ti (28 nm)/Pd (100 nm)/Au (200 nm) contacts were formed using magnetron sputtering on a diamond substrate heated to 350 °C. A set of test structures was prepared using photolithography to determine the contact resistance using the TLM method.

The NanoScope IIIa Dimension 3000™ SPM was employed for surface morphology characterization and for mapping local resistivity using SSRM. The SSRM measurements were performed in contact mode, applying solid platinum probes with a nominal tip radius of less than 20 nm. The Ti/Pd/Au planar contact was used as the ground electrode.

Confocal micro-Raman and PL imaging were carried out using the Horiba Jobin-Yvon T-64000 spectrometer, outfitted with an Olympus BX41 microscope and a motorized XYZ scanning stage. Raman measurements were made at ambient temperature using a backscattering geometry. The lines of KIMMON KOHA IK5651R-G He-Cd laser with the wavelengths 325 (3.82 eV) and 442 nm (2.81 eV) and the line of the Spectra-Physics EXLSR-532-150-CDRH solid-state laser with the wavelength 532 nm (2.33 eV) were used for excitation. The laser beam was focused onto the sample surface using a 100×/NA 0.9 objective, yielding a spot approximately 0.6 µm in diameter. A Linkam Scientific Instruments THMS600 micro-temperature cell cooled by liquid nitrogen was used to measure PL spectra at 77 K. Spatial 2D Raman and PL micro-mapping was performed using a motorized XYZ scanning table with a scanning step of 0.1 µm.
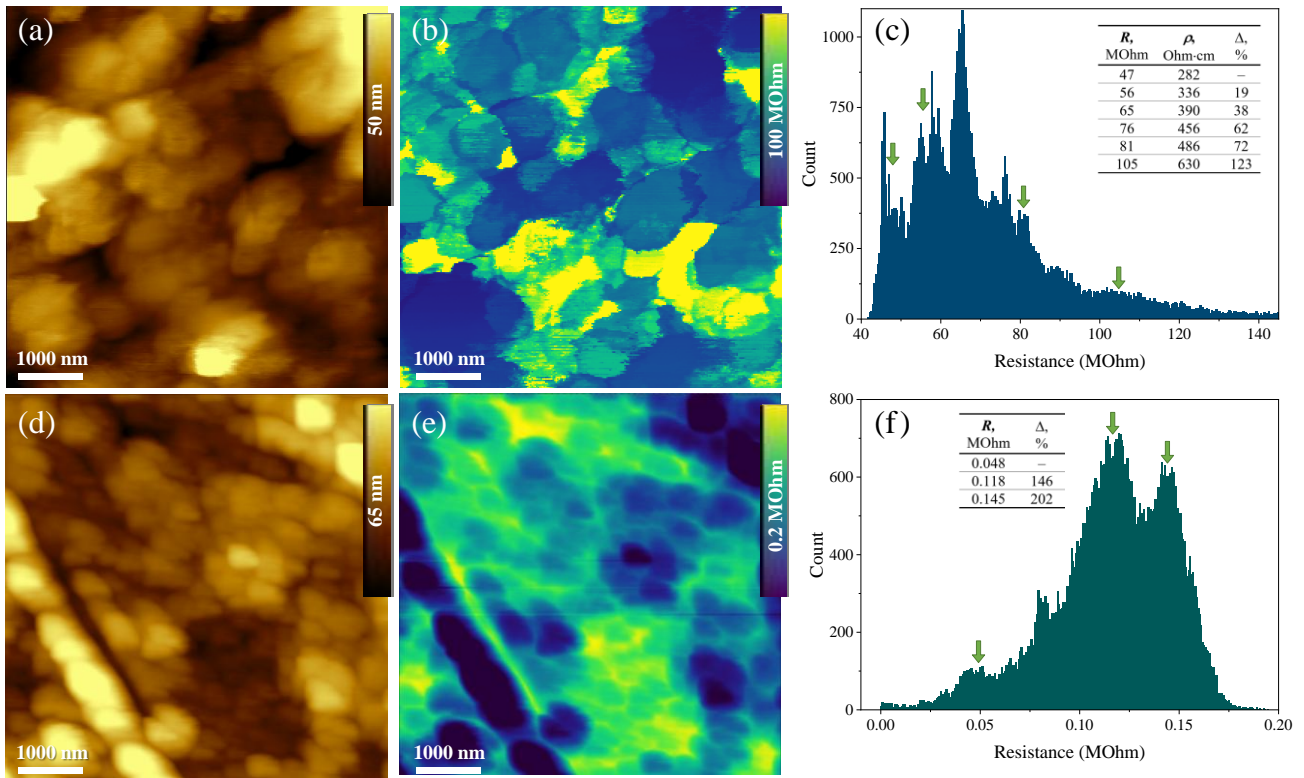
3. Results and discussion

In our previous studies of monocrystalline diamond materials, comprehensive experimental characterization precisely demonstrated the anisotropic doping in HPHT diamond crystals, with peak boron incorporation observed in the {111} growth sectors [27, 28]. Micro-FTIR mapping highlighted a pronounced, growth-sector-dependent distribution of uncompensated boron impurity, decreasing in concentration from approximately $7 \cdot 10^{18}$ cm^{-3} in {111} growth sectors down to around $2 \cdot 10^{17}$ cm^{-3} in {001} growth sectors. This trend was further corroborated by micro-Raman mapping, as evidenced by the relative intensity of additional phonon peaks associated with boron incorporation. The electronic properties of intersectoral boundaries were elucidated using scanning KPFM. Theoretical analysis suggests that the observed variation in the work function between the growth sectors is consistent with the increased boron doping (and elevated Fermi level position) in {111} as compared to {001} growth sectors, following the anticipated variations in boron doping. Furthermore, we examined the morphology and electrical properties of growth defects in boron-doped HPHT diamond crystals and multisectoral plates by using scanning probe microscopy techniques, complemented with micro-Raman and micro-FTIR mapping [28]. This comprehensive characterization elucidated the relationship between morphological defects, strain fields, boron distribution, and local electrical properties. Selective chemical etching was employed to uncover dislocation-related etch pits (EPs) on single crystal growth facets and
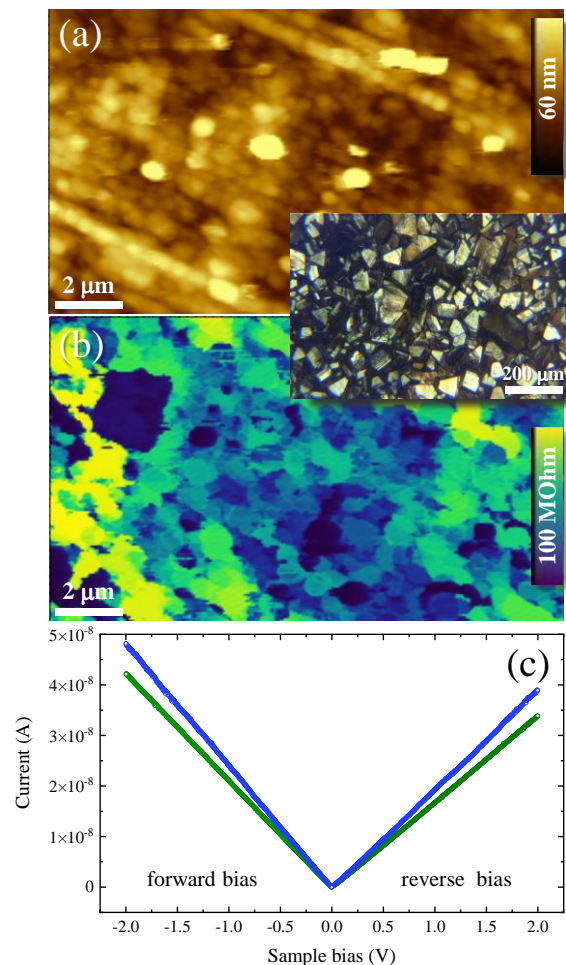
Fig. 1. (a) AFM height map and (b) corresponding SSRM resistance map of the CVD-grown BDD film. (c) Typical *I–V* curves from two randomly selected nano-grains. Inset: optical microscopy image showcasing micro-grains within the structure of CVD film.

Nikolenko A.S., Lytvyn P.M., Strelchuk V.V. et al. Impact of grain-dependent boron uptake on the nano-electrical …

378

Fig. 2. (a) AFM height map and (b) corresponding SSRM map for the BDD film. (d) AFM height map and (e) corresponding SSRM map for the BDD/Ti/Pd/Au multilayer contact. The associated histograms of resistance are presented in (c) for the BDD film and (f) for the multilayer contact.

plates sectioned in various orientations. EPs morphology and gradient densities were associated with underlying defects and variations in dislocation density.

Protrusions uniformly distributed on the plates were interpreted as manifestation of dislocations decorated by regions with lower boron concentrations, inferred from the selective etching rates. Micro-Raman mapping near the EPs revealed a diminished intensity and broadening of the diamond peak, suggesting an elevated boron concentration within the pits. The Raman frequency shifts indicated compressive/tensile strain fields surrounding the dislocations.

Moreover, SSRM revealed resistivity discrepancies at EPs and protrusions. Specifically, pits manifested a resistivity approximately 25% lower than that in growth sectors, whereas protrusions exhibited a resistivity 25% higher, denoting respective boron concentrations. These observations underscore the variations in localized electrical properties adjacent to dislocations. The findings advocate for the preferential utilization of (110)-oriented HPHT diamond, where dislocation-related current leakage defects are minimized.

This work explores the local structural properties and their corresponding nanoelectrical characteristics in CVD polycrystalline diamond films based on previously developed methodologies. The free-standing BDD samples were analyzed from the seed side. While the film volume contains crystallites with dimensions spanning tens of microns, as visualized by optical microscopy, the studied surface comprises nanocrystal grains ranging 200…800 nm in size (Fig. 1). A weak linear pattern remained after the mechanical polishing can be observed, yet the RMS value determined with AFM remains below 15 nm across a 15×15 μm field. The variations in resistance among individual grains and between grain clusters are depicted in the corresponding SSRM map (Fig. 1b). Notably, the resistance of the more pronounced surface features often exceeds that of the features in recessed regions. The fluctuations in resistance and height of the polished surface features are likely attributed to differences in boron dopant uptake. One would expect some reduction in resistance and mechanical hardness in diamond samples with higher boron concentrations. Representative current-voltage (*I–V*) curves from two arbitrarily chosen nanograins are presented in Fig. 1c, revealing a noticeable linear *I–V* relationship with minimal deviation based on the direction of the applied bias. Consequently, the electrical contact between the platinum SSRM tip and the CVD film is nearly ohmic.

The detailed SSRM maps are adduced in Fig. 2. There are no notable grain boundary features within the resistance data. Individual grains exhibit consistent resistance contrast, which can shift abruptly between

Nikolenko A.S., Lytvyn P.M., Strelchuk V.V. et al. Impact of grain-dependent boron uptake on the nano-electrical …

379

adjacent grains or grain clusters with similar resistance values. This observation agrees with previous studies, which suggest that grain boundaries manifest electrical activity primarily in the cases of low boron doping. Given a pseudo-ohmic tip-surface contact, where resistance remains unaffected by the applied voltage, and the appropriate selection of both bias voltage and tip-surface interaction force to mitigate parasitic resistance, the SSRM maps predominantly reflect the spreading resistance R. Under these conditions, the resistivity ρ can be expressed as $\rho = 4aR$, where a denotes the radius of the tip-surface contact. Simultaneously, the relationship between resistivity and carrier concentration $\rho = \left(q\left(n\mu_n + p\mu_p\right)\right)^{-1}$, where q represents the elementary charge, n/p – electron/hole concentration, and μ – associated mobility. Given these assumptions and presuming a prevailing hole concentration with consistent mobility, the SSRM maps can be interpreted as a qualitative representation of boron dopant distribution across individual grains in the CVD film. The resistance histogram in Fig. 2c distinctly showcases its multi-modal nature; the series of peaks potentially correlate with incremental shifts in boron content within the CVD diamond film grains. As detailed in the accompanying table inset, the relative resistance/resistivity variations between grains span from 20 up to 120%. Similar variations can be postulated for boron distribution across the film grains.

The same SSRM data were acquired on the Au surface of Ti/Pd/Au contact for comparison, as depicted in Fig. 2d–2f. The metal contact generally exhibits a comparable granular structure, with grain sizes ranging from 200 to 500 nm and resistance values that are three orders of magnitude lower. Through the fine structure of Au film, the large clusters of higher/lower resistance of BDD film are visible. The average size of these clusters is approximately 2 μm, and their shape directly aligns with the clusters formed by grains of analogous resistance within the diamond film. A notable feature of this metal contact film is the presence of high-resistance grain boundaries. This network of intergranular boundaries is clearly visible in Fig. 2e. The resistance of this network is 10…13% (~14 kOhm) higher than that in the central regions of the grains. The corresponding resistance histogram is also multimodal, although with fewer peaks. The specific resistance values of 50, 120 and 145 kOhm can be attributed to grains within the uppermost layer of the Au contact.

The described peculiarities revealed with SSRM can be addressed to inherent inhomogeneities of the diamond grown using the MPCVD method on non-native substrates. Boron doping facilitated with plasma sputtering is affected by many factors, including plasma temperature, ion concentration and the nuances of local crystalline growth. Crucially, the interrelation of morphological defects, strain fields and boron distribution play a significant role. Our prior research has indicated that regions surrounding dislocations possess diverse boron concentrations, probably resulting from the combined effects of strain fields and doping mechanisms. These defects and dislocations can modify local chemical potentials, rendering some areas more receptive to boron incorporation. The subsequent deposition of an Au film over a Ti/Pd barrier adds another layer of complexity. The Ti and Pd serve as anti-diffusion barriers, which could modify Au deposition behavior, potentially leading to distinct Au grain boundary configurations exhibiting increased resistance. The Pd, in particular, might induce the Au film nucleation and growth behavior, resulting in grain boundaries that are especially prone to conductivity disruptions. The Au film displays a granular structure with 200…500 nm grain sizes. These structures inherently possess grain boundaries where atomic configurations are less ordered. These transitional zones between grains can prevent electron movement, elevating resistance. Electron scattering increases at these boundaries, reducing electron mobility. Even with the Ti/Pd barrier in place, interactions between the BDD film and the overlying Au are distinguishable. The evident clusters of differential resistance from the BDD layer beneath the Au layer hint at possible charge interaction sites, which can modulate the resistance pattern of the Au layer above. This complex interplay of material properties, growth processes and subsequent interactions highlights the importance of multi-scale characterization in understanding and optimizing the performance of nanoscale materials and devices.
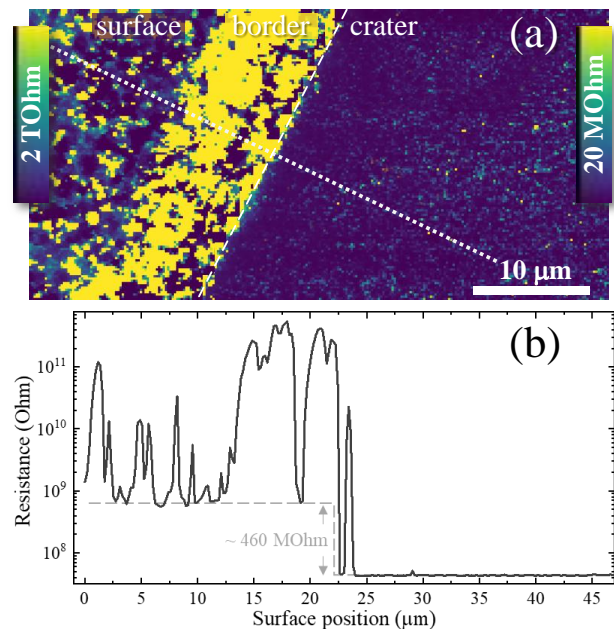

Fig. 3. (a) SSRM map of a BDD film fragment, depicting the surface post-metal contact deposition process (left side, labeled as "surface") and showcasing the side and bottom of a crater post-SIMS etching (right side, labeled as "border" and "crater"). (b) Presents the resistance profile along the indicated dotted line. Note that the SSRM map integrates two distinct scales on the left and right sides. The transition between these scales is delineated by a dashed line along the border/crater boundary.

Nikolenko A.S., Lytvyn P.M., Strelchuk V.V. et al. Impact of grain-dependent boron uptake on the nano-electrical …

380

The SSRM data revealed a difference of approximately 460 MOhm between the surface of the processed film and the subsurface layers of the BDD film sputtered *via* SIMS. Fig. 3 illustrates both the SSRM map and the corresponding linear profile of the BDD film post-metal contacts deposition, as well as the bottom of the SIMS-etched crater. The left portion of the SSRM map displays micron-sized clusters with varying resistance levels, including clusters with exceptionally high resistance values in the range of 10^{11} to 10^{12} Ohms. Notably, an ultra-high resistance band, approximately 10 µm in width, is observed along the boundary of the crater. This elevated resistance might be attributed to surface passivation or contamination during the contact processing. Furthermore, the clusters and the near-continuous band of ultra-high resistance can likely be traced back to the sputtering peculiarities of the BDD film during SIMS and its subsequent oxidation and passivation when being exposed to air caused by the reactive nature of a freshly sputtered surface. In contrast, the bottom region of the SIMS crater exhibits uniform resistance, consistent with that of the initial film.

The PL spectra (Fig. 4a) of the studied CVD sample at room temperature and excitation with the energy from the range 2.33...3.82 eV show emission bands typical for CVD diamond with nitrogen and boron impurities. In the PL spectra, besides the Raman F_{2g} band of diamond with a frequency of ~1330 cm^{-1}, radiation bands are recorded, usually attributed to the radiation of defective complexes with participation of nitrogen and boron impurities. Under excitation with the energy 2.33 eV, bands with the spectral positions 2.155 and 1.946 eV are present in these spectra, which are the zero-phonon lines (ZPL) of the NV^0 and NV^- nitrogen-vacancy centers, respectively, with a wide phonon sideband on the low-energy side.

When the excitation energy is increased up to 2.81 eV, the emission bands with the energies 2.65 and 2.59 eV are additionally recorded in the spectra (Fig. 4a), which in the samples co-doped with nitrogen and boron are attributed to the recombination of donor-acceptor pairs (DAP), where nitrogen is the donor, and boron is the acceptor [16, 29]. The ZPL 2.65 eV with a phonon sideband within the 2.45...2.6 eV region is attributed to the nearest neighbor nitrogen-boron pair $N_1^0 + B_1^0$ [16]. The band at 2.59 eV, by its spectral position, low half-width and sufficiently high intensity, can be attributed to the recombination of donor-acceptor pairs, which tentatively refers to split nitrogen-carbon interstitial associates with boron $(N_1C_1)_i B_1^-$ [16].
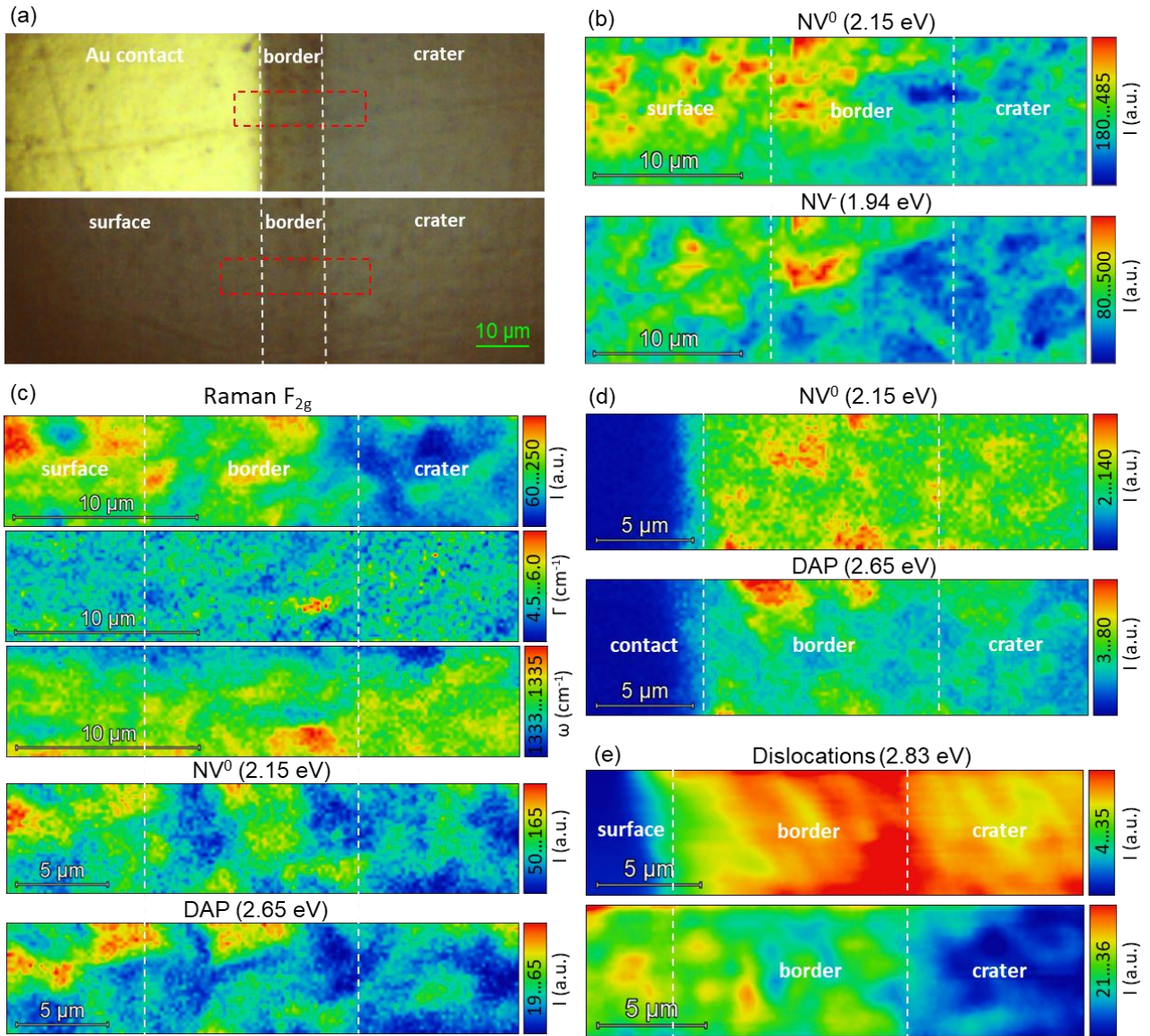
The nature of the broad emission band with the maximum near 2.32 eV (band B in Fig. 4) is not precisely known; in the literature, this band is associated with boron impurity in diamond, and its relative intensity increases with boron content in diamond, and at the concentrations up to ≲ 0.1 ppm it shows a fine structure, and at higher concentrations appears as one widened band [30].
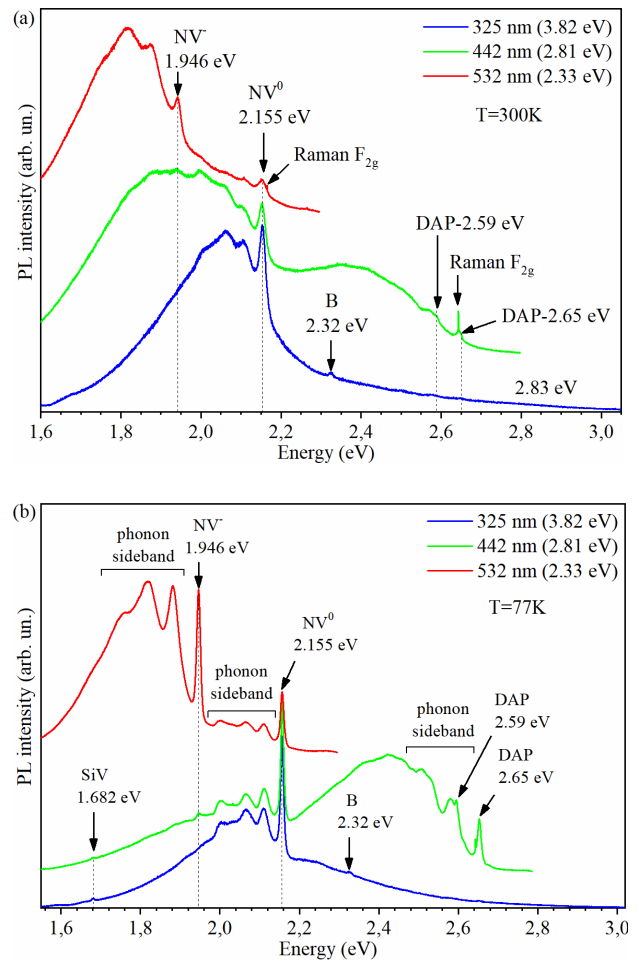
Fig. 4. PL spectra of the studied CVD diamond plate under excitation with the wavelengths 325 nm (3.82 eV), 442 nm (2.81 eV) and 532 nm (2.33 eV) at the temperatures 300 (a) and 77 K (b).

With a further increase in the excitation energy up to 3.81 eV (325 nm), redistribution of the intensity of the emission bands occurs in the PL spectra (Fig. 4), and a broad band with the energy close to 2.83 eV is recorded in the high-energy part of the spectrum, which, according to literature data, is caused by dislocations [30]. As expected, the temperature reduction down to 77 K (Fig. 4b) allowed us to distinguish the structure of the defective PL bands more clearly. Also, it revealed several additional emission bands. In particular, a PL band with the maximum of 1.682 eV is recorded in the spectra due to the defective center of SiV, which is considered promising for developing single-photon emitters [31–34]. As previously reported, the PL band of SiV centers has a non-monotonic intensity dependence on the concentration of Si in diamond with a gradual increase at low concentrations of silicon ~ $5 \cdot 10^{17}$ cm^{-3} and concentration damping at higher levels of doping, and also shows a significant enhancement in the region of non-epitaxial diamond inclusions, which is due to the peculiarity of their geometry and the spatial orientation of SiV centers

Nikolenko A.S., Lytvyn P.M., Strelchuk V.V. et al. Impact of grain-dependent boron uptake on the nano-electrical ...

381

Fig. 5. Optical image of the sample surface in the areas near the contact/crater and surface/crater boundaries, the areas of μ-PL and μ-Raman maps are marked in red (a); intensity distribution of PL bands of NV^0 and NV^- centers at the surface/crater boundary at $E_{exc} = 2.33$ eV (b); maps of the intensity, half-width and frequency of the Raman F_{2g} band of diamond, and the PL bands of the NV^0 and DAP centers at the surface/crater (c) and contact/crater (d) boundaries at $E_{exc} = 2.81$ eV; intensity distribution of the dislocation-induced PL band at 2.83 eV at the contact/crater and surface/crater boundaries at $E_{exc} = 3.82$ eV (e). $T = 300$ K.

along the $\langle 111 \rangle$ direction [17]. The intensity of this PL band is higher for the nucleation side of the sample (not shown here), which may indicate silicon atoms diffusion from the substrate into the CVD film during the growth process.

The relative intensity and shape of the PL bands related to defects differed for the spectra measured in different areas of the sample – on the surface, border and bottom of the SIMS crater. To find out the features of the spatial distribution of defects along the depth and surface of the CVD sample under study, we further carried out spatial 2D mapping of Raman and PL spectra at the boundary of the crater with a metal

contact and with the initial CVD surface (Fig. 5a). The area measured has been correlated to that shown in Fig. 3a.

The 2D maps (Fig. 5b–5d) of intensity distribution of the NV^0 (2.155 eV) and NV^- (1.940 eV) emission bands, as well as donor-acceptor pairs (DAP) bands at 2.65 eV (Fig. 5b–5d) revealed significant spatial hetero-geneity in the form of grains with a lateral size of the order of unities of micrometers with different intensity of PL bands, which is obviously caused by combined variation of crystal quality, defective and impurity composition in individual grains of a polycrystalline CVD film. In particular, this may be a sign of the

Nikolenko A.S., Lytvyn P.M., Strelchuk V.V. et al. Impact of grain-dependent boron uptake on the nano-electrical ...

382

different content of nitrogen and boron impurities in different grains of the polycrystalline film and at grain boundaries, which was previously observed by means of scanning photoelectron microscopy [35], high-resolution electron microscopy and electron energy loss spectroscopy (STEM-EELS), which showed a predominant embedding boron impurity in defective areas and on the boundaries of twins [36]. It should also be noted that the intensity maps of the PL bands of the NV^0 and NV^- centers (Fig. 5b) generally correlate with each other, while the NV^0 and DAP bands (Fig. 5d) show a certain anticorrelation, which reflects the heterogeneous conditions for the preferable incorporation of boron and nitrogen impurities and formation of different types of structural defects inside the growing CVD film.

The intensity distribution of the F_{2g} Raman band with a frequency of ~ 1332 cm^{-1} is also heterogeneous (Fig. 5c), which indicates spatial heterogeneity of the crystalline quality and impurity composition. A certain correlation is observed between intensity maps of Raman and PL bands: the higher intensity of the Raman band (better crystal quality) mainly corresponds to the lower intensity of the PL bands of defects (lower concentration of defects). The above observation also agrees with the correlations observed on the maps of the intensity, half-width and frequency of the Raman F_{2g} band (Fig. 5c), where the higher intensity corresponds to the lower half-width of the F_{2g} band, indicating better crystalline quality. On the other hand, the frequency position of the Raman band can depend on the content of defects and impurities, particularly boron and nitrogen, and on the strains developing with doping and having a non-uniform character at the grain boundaries. In general, doping with boron and nitrogen impurities at low concentrations can manifest itself in the Raman spectra as a decrease in intensity, a low-frequency shift and a broadening of the F_{2g} band due to an increase in the lattice constant and disordering [37, 38]. At higher boron content of ~$2 \cdot 10^{20}$ cm^{-3} (~ 1000 ppm) or higher, a decrease in the intensity, a low-frequency shift and asymmetric broadening of the F_{2g} peak is observed due to the Fano interaction between optical phonons and the electronic continuum [39, 40]. However, for CVD diamond films grown on Si substrates, residual compressive strains may develop upon cooling from the growth temperature to room temperature due to the difference in the coefficients of thermal expansion of the substrate and the film, which may further increase at high levels of boron doping (> 10,000 ppm) due to formation of secondary phases of graphite, amorphous carbon or excess boron at grain boundaries [24]. In our case, secondary carbon phases at grain boundaries were not registered. Therefore, it can be assumed that residual compressive deformations in the CVD film can cause the observed slight high-frequency shift of the F_{2g} band.

The spatial distribution of the intensity of the defective PL band with an energy of 2.83 eV (Fig. 5b–5c),

caused by dislocation-type defects, regardless of a particular spatial heterogeneity, did not reveal notable granular structure. Instead, the intensity of this PL band is higher on the surface of the CVD film and smaller in the crater and border areas. It can be assumed that this effect is caused by dislocations arising in the near-surface region of the diamond film during its mechanical processing (polishing). Instead, ion beam etching gradually removes the disturbed layers.

4. Conclusions

We have carried out a detailed examination of the influence of grain-dependent boron incorporation on both the nano-electrical and local optical properties of polycrystalline boron-doped CVD diamond films. Using the integrated approach combining scanning probe microscopy with optical Raman and photoluminescence micro-spectroscopy mapping, we were able to derive nuanced insights. Significant nanoscale variations in electrical resistance were identified among individual grains, spanning 200…800 nm laterally, and also between grain clusters. It has been interpreted as non-uniform boron dopant distribution across individual grains. Interestingly, the absence of noticeable resistive variations at grain boundaries has been ascertained to stem from a comparatively high level of boron doping.

The distinct multi-modal resistivity distribution, evident through a series of peaks and relative resistivity disparities (ranging from 20 up to 120%) between grains, alludes to the distribution of boron content inside these CVD diamond film grains. In juxtaposition, resistance maps of the Au surface of the Ti/Pd/Au contact showcased a granular morphology, grain dimensions oscillating between 200…500 nm, but with resistance figures markedly lower – three orders of magnitude in fact. Additionally, a discernible network of high-resistive boundaries was evident, presenting a resistance 10…13% elevated, as compared to their grain counterparts. Furthermore, substantial clusters showcasing pronounced resistance variability on the Au surface were determined to be influenced by the underlying diamond film grain clusters, which intriguingly modulated the Au layer resistance even in the presence of the Ti/Pd anti-diffusion barrier.

This interrelation of material characteristics, growth dynamics and ensuing interactions underscores the imperative of multiscale characterization, especially when the objective is comprehending and refining the efficacy of nanoscale materials and devices. Correlative confocal Raman and PL mapping, particularly through analysis of 2D maps elucidating the intensity, frequency, and linewidth of the Raman F_{2g} peak coupled with emission bands of specific nitrogen-vacancy centers and donor-acceptor pairs, reaffirmed pronounced spatial non-uniformities in grains. These non-uniformities were discerned to be closely linked with the amalgamated fluctuations in crystal quality and concentrations of both

Nikolenko A.S., Lytvyn P.M., Strelchuk V.V. et al. Impact of grain-dependent boron uptake on the nano-electrical …

383

boron and nitrogen impurities at both the granular and boundary levels. Conclusively, the distinct structural and nano-electrical traits observed in BDD films can be traced back to their intrinsic non-uniformities and the grain-specific boron uptake, a process significantly swayed by morphological irregularities and strain fields that adjust local chemical potentials, thus making certain zones more amenable to boron integration.

In summary, we propose an advanced monitoring approach for the MPCVD deposition process to achieve a more uniform boron doping distribution, which can potentially enhance the film overall electronic properties. Addressing the minimization of morphological defects and strain fields during deposition is crucial for ensuring a consistent and defect-free film. These efforts would ensure that local chemical potentials are uniformly distributed, leading to more homogeneous boron incorporation throughout the film. Furthermore, the optimized post-deposition annealing or other post-processing treatments can mitigate the adverse effects of inherent inhomogeneities, offering a more predictable and repeatable film quality, especially beneficial for device applications.

Acknowledgements

References

1. Alcantar-Peña J.J., de Obaldia E., Tirado P. *et al.* Polycrystalline diamond films with tailored micro/nanostructure/doping for new large area film-based diamond electronics. *Diam. Relat. Mater.* 2019. **91**. P. 261–271. https://doi.org/10.1016/j.diamond.2018.11.028.

2. Knittel P., Buchner F., Hadzifejzovic E. *et al.* Nanostructured boron doped diamond electrodes with increased reactivity for solar-driven CO_2 reduction in room temperature ionic liquids. *ChemCatChem.* 2020. **12**. P. 5548–5557. https://doi.org/10.1002/cctc.202000938.

3. Kunuku S., Ficek M., Wieloszynska A. *et al.* Influence of B/N co-doping on electrical and photo-luminescence properties of CVD grown homoepi-taxial diamond films. *Nanotechnology.* 2022. **33**. P. 125603. https://doi.org/10.1088/1361-6528/ac4130.

4. Liu D., Chen C., Perry D. *et al.* Facet-resolved electrochemistry of polycrystalline boron-doped diamond electrodes: Microscopic factors determining the solvent window in aqueous potassium chloride solutions. *ChemElectroChem.* 2018. **5**. P. 3028–3035. https://doi.org/10.1002/celc.201800770.

5. Ullah M., Manzoor R.A., Ahmed E. Electrical conductivity of CVD diamond thin films, in: *Micro Nanomanufacturing*, Vol. II, Springer Int. Publ., Cham, 2018. P. 337–412. https://doi.org/10.1007/978-3-319-67132-1_13.

6. Szunerits S., Mermoux M., Crisci A. *et al.* Raman imaging and Kelvin probe microscopy for the examination of the heterogeneity of doping in polycrystalline boron-doped diamond electrodes. *J. Phys. Chem. B.* 2006. **110**. P. 23888–23897. https://doi.org/10.1021/jp064429.

7. Wilson N.R., Clewes S.L., Newton M.E., Unwin P.R., Macpherson J.V. Impact of grain-dependent boron uptake on the electrochemical and electrical properties of polycrystalline boron doped diamond electrodes. *J. Phys. Chem. B.* 2006. **110**. P. 5639–5646. https://doi.org/10.1021/jp0547616.

8. Watanabe T., Yoshioka S., Yamamoto T. *et al.* The local structure in heavily boron-doped diamond and the effect this has on its electrochemical properties. *Carbon.* 2018. **137**. P. 333–342. https://doi.org/10.1016/j.carbon.2018.05.026.

9. Ullah M., Ahmed E., Hussain F. *et al.* Electrical conductivity enhancement by boron-doping in diamond using first principle calculations. *Appl. Surf. Sci.* 2015. **334**. P. 40–44. https://doi.org/10.1016/j.apsusc.2014.07.157.

10. Ternyak O., Cimmino A.A., Prawer S., Hoffman A. Ultrathin continuous undoped diamond films: Investigation of nanoscale conduction properties. *Diam. Relat. Mater.* 2005. **14**, issue 3–7. P. 272–278. https://doi.org/10.1016/j.diamond.2005.01.043.

11. Monteiro O.R. Structural defects and sp2 localization in CVD diamond. *J. Mater. Sci.* 2019. **54**. P. 2300–2306. https://doi.org/10.1007/s10853-018-2949-1.

12. Xu Z., Hantschel T., Tsigkourakos M., Vandervorst W. Scanning spreading resistance microscopy for electrical characterization of diamond interfacial layers. *phys. status solidi (a).* 2015. **212**. P. 2578–2582. https://doi.org/10.1002/pssa.201532234.

13. Zhang L., Koike M., Ono M.*et al.* Comprehensive 2D-carrier profiling of low-doping region by high-sensitivity scanning spreading resistance microscopy (SSRM) for power device applications. *Microelectron. Reliab.* 2015. **55**. P. 1559–1563. https://doi.org/10.1016/j.microrel.2015.06.142.

14. Ryl J., Cieslik M., Zielinski A. *et al.* High-temperature oxidation of heavy boron-doped diamond electrodes: microstructural and electrochemical performance modification. *Materials* (Basel). 2020. **13**. P. 964. https://doi.org/10.3390/ma13040964.

15. Zaitsev A.M. *Optical Properties of Diamond.* Springer Berlin Heidelberg, 2001. https://doi.org/10.1007/978-3-662-04548-0.

Nikolenko A.S., Lytvyn P.M., Strelchuk V.V. et al. Impact of grain-dependent boron uptake on the nano-electrical ...

384

16. Dischler B., Rothemund W., Maier K. *et al.* Diamond luminescence: Resolved donor-acceptor pair recombination lines. *Diam. Relat. Mater.* 1994. **3**. P. 825–830.
https://doi.org/10.1016/0925-9635(94)90278-X.

17. Bolshakov A., Ralchenko V., Sedov V. *et al.* Photo-luminescence of SiV centers in single crystal CVD diamond *in situ* doped with Si from silane. *phys. status solidi* (*a*). 2015. **212**. P. 2525–2532. https://doi.org/10.1002/pssa.201532174.

18. Schreyvogel C., Polyakov V., Wunderlich R., Meijer J., Nebel C.E. Active charge state control of single NV centres in diamond by in-plane Al-Schottky junctions. *Sci. Rep.* 2015. **5**. P. 12160. https://doi.org/10.1038/srep12160.

19. Osterkamp C., Mangold M., Lang J. *et al.* Engi-neering preferentially-aligned nitrogen-vacancy centre ensembles in CVD grown diamond. *Sci. Rep.* 2019. **9**. P. 5786.
https://doi.org/10.1038/s41598-019-42314-7.

20. de Oliveira F., Antonov D., Wang Y. *et al.* Tailoring spin defects in diamond by lattice charging. *Nat. Commun.* 2017. **8**. P. 15409. https://doi.org/10.1038/ncomms15409.

21. Wurzinger P., Pongratz P., Hartmann P., Haubner R., Lux B. Investigation of the boron incorporation in polycrystalline CVD diamond films by TEM, EELS and Raman spectroscopy. *Diam. Relat. Mater.* 1997. **6**. P. 763–768.
https://doi.org/10.1016/S0925-9635(96)00668-1.

22. Paprocki K., Dittmar-Wituski A., Trzciński M. *et al.* The comparative studies of HF CVD diamond films by Raman and XPS spectroscopies. *Opt. Mater.* 2019. **95**. P. 109251.
https://doi.org/10.1016/j.optmat.2019.109251.

23. Habka N., Barjon J., Lazea A., Haenen K. Stress in (110)-textured phosphorus-doped polycrystalline diamond studied by Raman and cathodolumi-nescence spectroscopies. *J. Appl. Phys.* 2010. **107**. P. 103521 (4 p.) https://doi.org/10.1063/1.3428452.

24. Ferreira N.G., Abramof E., Corat E.J. *et al.* Stress study of HFCVD boron-doped diamond films by X-ray diffraction measurements. *Diam. Relat. Mater.* 2001. **10**. P. 750–754.
https://doi.org/10.1016/S0925-9635(00)00522-7.

25. Dub M.M., Kudryk Y.Y. Heat-resistant ohmic contact system to polycrystalline diamond. *2018 IEEE 8th Int. Conf. Nanomaterials: Application & Properties (NAP)*, Zatoka, Ukraine, 2018. P. 1–4. https://doi.org/10.1109/NAP.2018.8915003.

26. Dub M.N. Electrophysical parameters of Au-Ti oh-mic contacts to polycrystalline diamond. *2017 IEEE 7th Int. Conf. Nanomaterials: Application & Properties (NAP)*, Odessa, Ukraine, 2017. P. 02NTF22-1–3.
https://doi.org/10.1109/NAP.2017.8190380.

27. Nikolenko A.S., Strelchuk V.V., Lytvyn P.M. *et al.* Correlated Kelvin-probe force microscopy, microFTIR and micro-Raman analysis of doping anisotropy in multisectorial boron-doped HPHT diamonds. *Diam. Relat. Mater.* 2022. **124**. P. 108927.
https://doi.org/10.1016/j.diamond.2022.108927.

28. Lytvyn P.M., Strelchuk V.V., Nikolenko A.S. *et al.* Electrostructural and morphological features of etch pits in boron-doped HPHT-diamond single crystals and multisectoral plates. *Diam. Relat. Mater.* 2023. **133**. P. 109752.
https://doi.org/10.1016/j.diamond.2023.109752.

29. Dischler B. *Handbook of Spectral Lines in Diamond.* Springer Berlin Heidelberg, 2012. https://doi.org/10.1007/978-3-642-22215-3.

30. Ruan J., Kobashi K., Choyke W.J. On the "band-A" emission and boron related luminescence in diamond. *Appl. Phys. Lett.* 1992. **60**. P. 3138–3140. https://doi.org/10.1063/1.106748.

31. Khramtsov I.A., Fedyanin D.Y. Bright single-photon emitting diodes based on the silicon-vacancy center in AlN/Diamond heterostructures. *Nanomaterials.* 2020. **10**. P. 361.
https://doi.org/10.3390/nano10020361.

32. Aharonovich I., Englund D., Toth M. Solid-state single-photon emitters. *Nat. Photonics.* 2016. **10**. P. 631–641. https://doi.org/10.1038/nphoton.2016.186.

33. Neu E., Steinmetz D., Riedrich-Möller J. *et al.* Single photon emission from silicon-vacancy colour centres in chemical vapour deposition nano-dia-monds on iridium. *New J. Phys.* 2011. **13**. P. 025012. https://doi.org/10.1088/1367-2630/13/2/025012.

34. Wang C., Kurtsiefer C., Weinfurter H., Burchard B. Single photon emission from SiV centres in diamond produced by ion implantation. *J. Phys. B. – At. Mol. Opt.* 2006. **39**. P. 37–41. https://doi.org/10.1088/0953-4075/39/1/005.

35. Zakharov A.A., Ralchenko V., Khmelnitskii R., Lindau I. Scanning photoelectron microscopy study of as-grown and heat-treated chemical vapor deposition boron-doped diamond films. *J. Vac. Sci. Technol. B.* 2002. **20**. P. 2509.
https://doi.org/10.1116/1.1525009.

36. Lu Y.-G., Turner S., Verbeeck J. *et al.* Direct visualization of boron dopant distribution and coordination in individual chemical vapor deposition nanocrystalline B-doped diamond grains. *Appl. Phys. Lett.* 2012. **101**. P. 041907. https://doi.org/10.1063/1.4738885.

37. Brunet F., Germi P., Pernet M. *et al.* The effect of boron doping on the lattice parameter of homoepitaxial diamond films. *Diam. Relat. Mater.* 1998. **7**. P. 869–873. https://doi.org/10.1016/S0925-9635(97)00316-6.

38. Surovtsev N.V., Kupriyanov I.N., Malinovsky V.K. *et al.* Effect of nitrogen impurities on the Raman line width in diamonds. *J. Phys. Condens. Matter.* 1999. **11**. P. 4767–4774.
https://doi.org/10.1088/0953-8984/11/24/316.

Nikolenko A.S., Lytvyn P.M., Strelchuk V.V. et al. Impact of grain-dependent boron uptake on the nano-electrical …

385

39. Utyuzh A.N., Timofeev Y.A., Rakhmanina A.V. Effect of boron impurity on the Raman spectrum of synthetic diamond. *Inorg. Mater.* 2004. **40**. P. 926–931. https://doi.org/10.1023/B:INMA.0000041323.35298.dd.

40. Srimongkon K., Ohmagari S., Kato Y. *et al.* Boron inhomogeneity of HPHT-grown single-crystal diamond substrates: Confocal micro-Raman mapping investigations. *Diam. Relat. Mater.* 2016. **63**. P. 21–25. https://doi.org/10.1016/j.diamond.2015.09.014.

Authors and CV

Andrii S. Nikolenko, PhD, Deputy Head of Department at the V. Lashkaryov Institute of Semiconductor Physics, NASU. Field of research: semiconductor physics, semiconductor nanostructures and heterostructures, Raman, photoluminescence and FTIR spectroscopy. https://orcid.org/0000-0001-6775-3451

Petro M. Lytvyn, PhD in Physics and Mathematics, Head of Department at the V. Lashkaryov Institute of Semiconductor Physics, NASU. The area of scientific interests covers nanophysics of semiconductors and related materials. E-mail: plyt2007@gmail.com https://orcid.org/0000-0002-0131-9860

Viktor V. Strelchuk, Doctor of Science in Physics and Mathematics, Professor, Leading Researcher at the Laboratory of submicron optical spectroscopy, V. Lashkaryov Institute of Semiconductor Physics. Authored over 300 publications, 10 patents, 6 textbooks. Field of research: physics of semiconductors, Raman and photoluminescence spectroscopy of semiconductors, nanostructures and nanoscale materials. E-mail: viktor.strelchuk@ccu-semicond.net, https://orcid.org/0000-0002-6894-1742

Tetiana V. Kovalenko, PhD, Senior Researcher at the V. Bakul Institute for Superhard Materials, NASU. The area of her scientific interests covers: solution-melt crystallization of diamond at high pressures and temperatures, temperature gradient method, phase transformations at high pressures, semiconductors, morphology. She is the author of more than 60 science papers and technical patents. E-mail: tetiana.v.kovalenko@gmail.com, https://orcid.org/0000-0003-4878-5161

Igor M. Danylenko, PhD student at the V. Lashkaryov Institute of Semiconductor Physics. The area of scientific interests covers Raman, PL and FTIR spectroscopy of semiconductor nanostructures, optical, phonon and electrical properties of semiconductors and, in particular, of semiconducting diamond crystals. E-mail: igor.tesV@gmail.com, https://orcid.org/0000-0002-8740-204X

Sergii V. Malyuta, PhD, Teaching Assistant at National Technical University of Ukraine "Igor Sikorsky Kyiv Polytechnic Institute". The area of scientific interests covers scanning probe microscopy (SPM), in particular, atomic force microscopy, Kelvin-probe force microscopy, morphological properties of semiconductors and nanostructures, diamond, SPM data processing and analysis. E-mail: serhiy.malyuta@gmail.com, https://orcid.org/0000-0003-0466-9900

Yaroslav Ya. Kudryk, PhD, Senior Researcher at the V. Lashkaryov Institute of Semiconductor Physics. The area of his scientific interests includes solid state physics, transport properties in metal-semiconductor contacts to SiC, GaN, GaP, InP and diamond. E-mail: kudryk@isp.kiev.ua, https://orcid.org/0000-0002-5551-2922

Yuriy Yu. Stubrov, Junior Researcher at the V. Lashkaryov Institute of Semiconductor Physics. The area of scientific interests covers optical, phonon, electrical properties of diamond and carbon nanostructures and their study by using optical, Raman and PL microspectroscopy methods. E-mail: yurii.stubrov@gmail.com, https://orcid.org/0000-0001-7059-9424

Sergii O. Ivakhnenko, Professor, Doctor of Technical Sciences, Corresponding member of NAS of Ukraine. The area of his scientific interests covers phase transformations in elements and materials at high pressures and high temperatures, nucleation and growth kinetics of diamond single crystals in solution-melt systems at high pressure and high temperature. He is the author of more than 300 scientific papers and technical patents. E-mail: sioz@ismv13.kiev.ua, https://orcid.org/0000-0002-4796-3416

Nikolenko A.S., Lytvyn P.M., Strelchuk V.V. et al. Impact of grain-dependent boron uptake on the nano-electrical ...

386

Authors' contributions

Вплив вбудовування бору в кристалічні зерна на наноелектричні та локальні оптичні властивості легованого бором полікристалічного CVD-алмазу

А.С. Ніколенко, П.М. Литвин, В.В. Стрельчук, І.М. Даниленко, С.В. Малюта, Я.Я. Кудрик, Ю.Ю. Стубров, Т.В. Коваленко, С.О. Івахненко

Анотація. Леговані бором алмазні полікристалічні плівки (BDD), отримані методом хімічного осадження з парової фази (CVD), мають унікальні електричні та оптичні властивості, зумовлені нерівномірним вбудовуванням бору в зерна плівки. У роботі з використанням методів скануючої зондової мікроскопії та конфокальної мікроспектроскопії досліджено вплив легування бором на локальні наноелектричні та оптичні властивості плівок BDD. Об'єм плівок BDD складався з кристалітів розміром у кілька десятків мікрон, а поверхня – із зерен розміром 200…800 нм. Скануюча мікроскопія опору розтікання (SSRM) виявила суттєві варіації електричного опору зерен на нанорівні, що пов'язано з особливостями нерівномірного вбудовування бору. На картах SSRM не виявлено особливостей опору, пов'язаних із міжзеренними границями, що є типовим для плівок із високим вмістом бору $\sim 3\cdot10^{19}$ см$^{-3}$. Аналіз SSRM поверхні Au контакту BDD/Ti/Pd/Au виявив подібну зернисту морфологію поверхні, але з опором нижчим на три порядки. Для верхнього шару золота вже є характерним наявність чітко виокремлених міжзеренних границь. Спостережувана мережа міжзеренних границь із підвищеним опором корелює з кластерами зерен BDD. Фотолюмінесцентна спектроскопія показала смуги азотно-вакансійних центрів та донорно-акцепторних пар. Конфокальне раманівське та фотолюмінесцентне картування виявили значну просторову неоднорідність у вигляді зерен мікрометрового масштабу щодо структурної якості кристалів та концентрації бору та азоту внаслідок їх неоднорідного вбудовування. Виявлені структурні та наноелектричні особливості BDD-плівок зумовлено неоднорідностями росту та вбудовуванням бору в кристалічні зерна плівки, вплив яких посилюється дефектами та деформаційними полями, що змінюють локальні хімічні потенціали. Отримані результати є важливими для поглибленого розуміння шляхів оптимізації електричних і оптичних характеристик BDD-плівок, що мають значний потенціал в електронних, електрохімічних та квантових застосуваннях.

Ключові слова: легований бором CVD-алмаз, фотолюмінесценція, раманівська спектроскопія, скануюча мікроскопія опору розтікання, оптичні, електричні та структурні властивості.